ADVANCED MATERIALS
www.advmat.de

Sr-Doped Superionic Hydrogen Glass: Synthesis and Properties of SrH_{22}

Dmitrii V. Semenok, Wuhao Chen, Xiaoli Huang, Di Zhou, Ivan A. Kruglov, Arslan B. Mazitov, Michele Galasso, Christian Tantardini, Xavier Gonze, Alexander G. Kvashnin,* Artem R. Oganov, and Tian Cui**

Recently, several research groups announced reaching the point of metallization of hydrogen above 400 GPa. Despite notable progress, detecting superconductivity in compressed hydrogen remains an unsolved problem. Following the mainstream of extensive investigations of compressed metal polyhydrides, here small doping of molecular hydrogen by strontium is demonstrated to lead to a dramatic reduction in the metallization pressure to ≈200 GPa. Studying the high-pressure chemistry of the Sr–H system, the formation of several new phases is observed: *C*2/*m*-Sr_3H_{13}, pseudocubic SrH_6, SrH_9 with cubic $F\bar{4}3m$-Sr sublattice, and pseudo tetragonal superionic *P*1-SrH_{22}, the metal hydride with the highest hydrogen content (96 at%) discovered so far. High diffusion coefficients of hydrogen in the latter phase $D_H = 0.2–2.1 \times 10^{-9}$ m^2 s^{-1} indicate an amorphous state of the H-sublattice, whereas the strontium sublattice remains solid. Unlike Ca and Y, strontium forms molecular semiconducting polyhydrides, whereas calcium and yttrium polyhydrides are high-T_C superconductors with an atomic H sublattice. The discovered SrH_{22}, a kind of hydrogen sponge, opens a new class of materials with ultrahigh content of hydrogen.

1. Introduction

Reaching the metallic state of pure molecular hydrogen by compression is one of the most spectacular challenges in high-pressure physics and chemistry. Studies of hydrogen metallization[1–3] have been in the focus since the 1990s, with the experimental metallization limit moving step by step from 150[4] to 430–500 GPa.[1,5] A consistent increase in pressure leads to a series of phase transitions in solid hydrogen (phases I–V[1,5]), gradual quenching of the Raman signals, and darkening of the sample down to a complete loss of transparency. Despite a significant progress in achieving ultrahigh pressures in the last five years, detecting superconductivity of metallic hydrogen remains an unsolved problem. Studies of the electrical conductivity at pressures above 400 GPa remain very challenging.

In 2004, N. Ashcroft suggested that the precompression effects caused by chemical bonding to other atoms may help to convert hydrogen to a metallic state. Fifteen years later, this idea was confirmed in the synthesis of many metallic and superconducting hydrides such as H_3S,[6,7] LaH_{10},[8,9] YH_6,[10,11] YH_9,[11,12] ThH_{10},[13] CeH_9,[14] PrH_9,[15] NdH_9,[16] and so forth. It is believed now that the superconducting properties of these compounds are due to the presence of a sublattice of metallic hydrogen, which is formed in pure hydrogen only at pressures of 500–700 GPa.

There must be an intermediate link between these two forms of hydrogen, metallic and superconducting, and a molecular

D. V. Semenok, D. Zhou, M. Galasso, X. Gonze, A. G. Kvashnin, A. R. Oganov
Skolkovo Institute of Science and Technology
Bolshoy Boulevard, 30/1, Moscow 121205, Russia
E-mail: A.Kvashnin@skoltech.ru

W. Chen, X. Huang, T. Cui
State Key Laboratory of Superhard Materials
College of Physics
Jilin University
Changchun 130012, China
E-mail: huangxiaoli@jlu.edu.cn

I. A. Kruglov, A. B. Mazitov
Dukhov Research Institute of Automatics (VNIIA)
Moscow 127055, Russia

I. A. Kruglov, A. B. Mazitov
Moscow Institute of Physics and Technology
9 Institutsky Lane, Dolgoprudny 141700, Russia

C. Tantardini
UiT The Arctic University of Norway
PO Box 6050 Langnes, Troms N-9037, Norway

C. Tantardini
Institute of Solid State Chemistry and Mechanochemistry SB RAS
Novosibirsk 630128, Russian Federation

X. Gonze
European Theoretical Spectroscopy Facility
Institute of Condensed Matter and Nanosciences
Université Catholique de Louvain
Chemin des étoiles 8, bte L07.03.01, Louvain-la-Neuve B-1348, Belgium

T. Cui
School of Physical Science and Technology
Ningbo University
Ningbo 315211, China
E-mail: cuitian@nbu.edu.cn

The ORCID identification number(s) for the author(s) of this article can be found under https://doi.org/10.1002/adma.202200924.

DOI: 10.1002/adma.202200924

dielectric or semiconducting phase. Moreover, this "bridge", a molecular metal hydride, has been found. In 2015–2017, it has been shown that lithium and sodium form molecular nonconducting hydrides LiH_6[17] and NaH_7.[18] Continuing these studies, we have recently synthesized a unique barium superhydride BaH_{12}[19] which is a molecular metal and a superconductor at moderate pressures of 120–140 GPa. Pure hydrogen should demonstrate such properties at pressures above 350 GPa during the transition between the semiconducting and metallic modifications due to the band overlap. This insulator-to-metal transition (also called the Wigner–Huntington transition[20]) has never been observed and repeated before for either hydrogen or hydrides. Looking from a different perspective, BaH_{12} is almost pure hydrogen doped by 8 at% of barium ($Ba_{0.08}H_{0.92}$). This kind of electron doping brings the Wigner–Huntington transition closer and allows us (at very moderate pressures) to see what happens with pure hydrogen at more extreme conditions.

In this work, we investigated chemical reactions of strontium and strontium dihydride with hydrogen at high pressures (up to 181 GPa) and temperatures. In addition to a series of new molecular polyhydrides with compositions Sr_3H_{13}, SrH_6, and $SrH_{\approx 9}$, we discovered an amazing compound with a tetragonal strontium sublattice and the chemical formula SrH_{22}, which is hydrogen doped by 4 atom percentage of Sr. It is a yellow-colored semiconductor at 140 GPa. Together with BaH_{12}, this novel polyhydride, a successful model of hydrogen metallization via doping leading to the band overlap, does not require multi-megabar pressures and can be studied using a wide range of physical methods.

2. Results and Discussions

2.1. Structure Prediction and Synthesis of SrH_{22}

At the first stage of the research, we reexamined the Sr—H system at pressures of 50–200 GPa using the USPEX code.[21–23] From the chemical point of view, strontium has many of the characteristics of barium, which, as has been shown in our recent work,[19] reacts with hydrogen to form dodecahydride BaH_{12}. One of the goals of this research was to study the possibility of formation of similar strontium polyhydrides with the composition SrH_{12} or higher.

An evolutionary search using USPEX for thermodynamically stable phases in the Sr—H system (**Figure 1**, and Figures S1 and S2, Supporting Information) shows that this system is very rich in various compounds. At 150 GPa and 0 K (Figure 1f), there are several strontium hydrides on the convex hull: well-known *P*6/*mmm*-SrH_2; pseudocubic *P*1-SrH_6 (or Sr_8H_{48}) similar to recently discovered Eu_8H_{46}[24] and Ba_8H_{46};[25] superhydrides

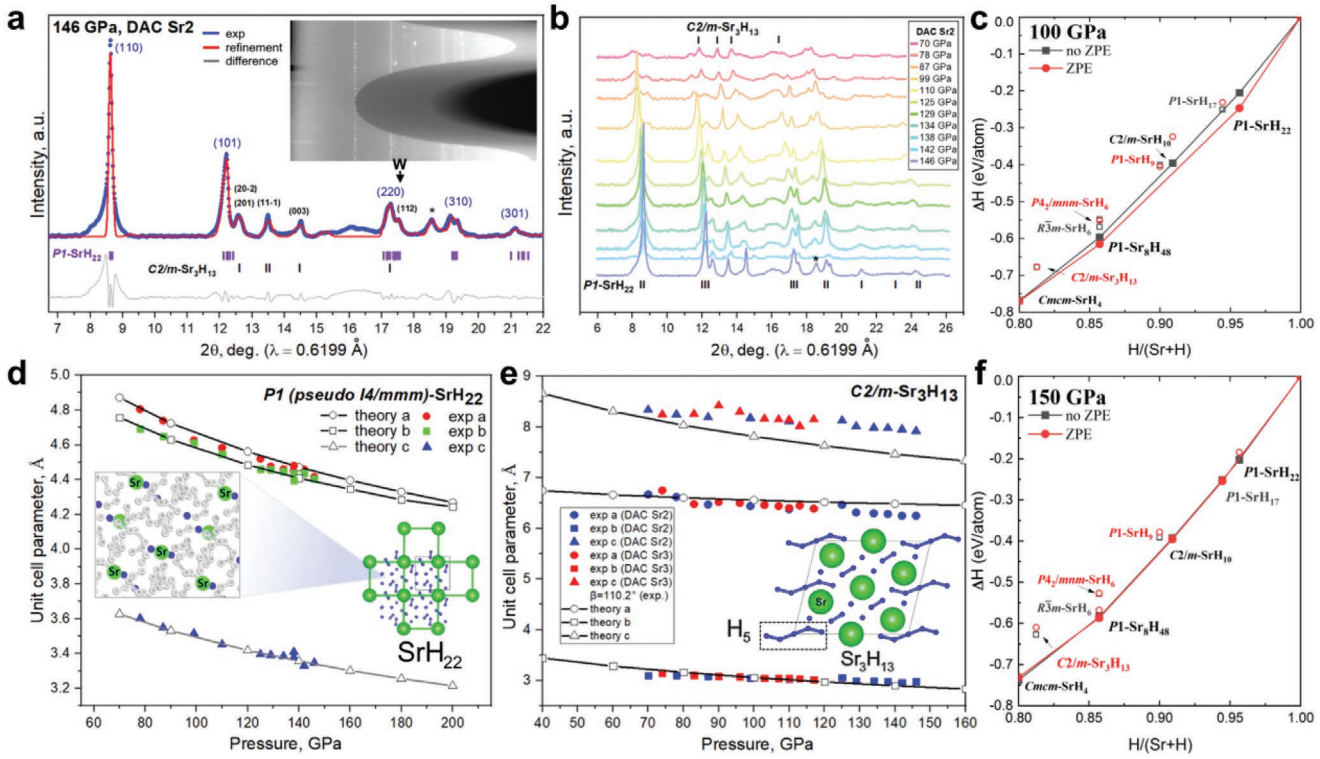

Figure 1. X-ray diffraction (XRD) study of strontium hydrides in DAC Sr2. a) Experimental XRD pattern and the Le Bail refinements of the unit cell parameters of pseudotetragonal *P*1-SrH_{22} and monoclinic *C*2/*m*-Sr_3H_{13} at 146 GPa. The experimental data, fit, and residues are shown in blue, red, and gray, respectively. Unidentified reflections are indicated by asterisks. The broadening of the (110) reflection is related to the proximity to the edge of WC seat. The inset shows the 2D diffraction image. b) XRD patterns obtained during decompression of DAC Sr2 from 146 to 70 GPa. c,f) Convex hulls of the Sr—H system at 100 and 150 GPa calculated with and without the zero-point energy (ZPE) contribution at 0 K. d,e) Experimental and theoretical dependences of the unit cell parameters on the pressure for *P*1-SrH_{22} (d) and *C*2/*m*-Sr_3H_{13} (e). Insets: Crystal structures of SrH_{22} (the blue circles indicate isolated H atoms) and Sr_3H_{13}.

$C2/m$-SrH_{10} and $P1$-SrH_{17}. At 100 GPa (Figure 1c), lower hydrides $Cmmm$-SrH and $Cmcm$-SrH_4 are stable, as well as Sr_8H_{48} and superhydride $P1$-SrH_{22}, whose structure is described below. Surprisingly, even at low pressures, there is wide variety of stable or slightly metastable (<30 meV per atom from the convex hull) higher strontium polyhydrides, in agreement with previous studies[26] (Figure S1, Supporting Information). This indicates a high probability of discovering new compounds in the strontium–hydrogen system even at low pressures.

We first experimentally investigated chemical reactions of strontium with hydrogen at pressures above 1 Mbar. The analysis of the X-ray diffraction patterns (Figure 1a,b) shows that a mixture of two strontium hydrides is formed after the laser heating of Sr with ammonia borane (AB) in DAC Sr2 (Table S1, Supporting Information) at 146 GPa, with a predominance of the phase having the *bct* tetragonal set of reflections (Figure 1a) and a very large unit cell volume. The comparison with USPEX calculations shows that the main phase can be immediately ascribed to pseudotetragonal $P1$-SrH_{22} with a unit cell volume of 65.1 Å^3/Sr at 100 GPa and temperature 0 K. At this pressure, the H sublattice of $P1$-SrH_{22} consists of H_2 molecules and H^- anions, and the minimum H−H bond length is d(H−H) = 0.76 ± 0.02 Å. The best candidate for the second phase, monoclinic $C2/m$-Sr_3H_{13}, with a unit cell volume of 25.26 Å^3/Sr at 100 GPa, was found to be 60 meV per atom above the convex hull. For both phases, the predicted diffraction patterns, equation of state, and pressure dependence of the unit cell parameters are in very close agreement with the experimental data (Figure 1d,e). A similar situation was observed in DAC Sr1 (Table S1, Supporting Information) loaded with SrH_2/AB, where an XRD pattern characteristic for SrH_{22} was detected at 138 GPa with a minimum amount of impurities (Figure S25, Supporting Information). For this reason, DAC Sr1 was used for subsequent optical and Raman measurements.

Molecular polyhydrides are not something entirely new in the chemistry of hydrogen. In 2009, the formation of other molecular van der Waals polyhydride $Xe(H_2)_{7–8}$ was confirmed using single-crystal X-ray diffraction as well as IR and Raman spectroscopy in a Xe−H_2 mixture at 5 GPa.[27] This discovery had been followed by an investigation of $(HI)(H_2)_{13}$ obtained as a small impurity in $HI(H_2)$ after the laser heating of the $H_2 + I_2$ mixture above 25 GPa.[28] A significant difference of strontium hydrides from xenon and iodine (HI) polyhydrides is a strong charge transfer and polarization of the Sr−H bonds. Indeed, Bader charge analysis performed in accordance with our previous experience[29,30] (Table S9, Supporting Information) shows that the Sr atoms are a source of electrons for hydrogen. The charge of the strontium atoms in SrH_{22} is +1.23|e| at 120 GPa, whereas most of the H_2 molecules have a small negative charge (−0.1|e|). About 10% of the H atoms are solitary anions H^- with a charge of −0.32|e| (Inset in Figure 1d, blue circles). As we will see later, these anions play an important role in the conductivity of this compound, making it a superionic hydride. Further theoretical study shows that anharmonic effects stabilize the structure of SrH_{22} at 100 GPa (Figure S13, Supporting Information). Calculations of the band structure point to a pronounced bandgap of 1.5–1.9 eV in this material at 120 GPa. According to theoretical predictions, increasing pressure above 200 GPa leads to metallization of the molecular H-sublattice via the band overlap and emergence of superconductivity with T_C = 21 K (μ^* = 0.1, Figure S14, Supporting Information).

Optical properties of $P1$-SrH_{22} were studied in DAC Sr1 at 100–135 GPa. In transmitted light, this superhydride has a yellow or orange color at 100 GPa with the maximum transmission of 630 nm wavelength. Increasing the pressure to 131 GPa leads to a significant darkening of the sample that corresponds to the gradual closure of the bandgap (Figure S34, Supporting Information). The Raman spectra, measured using a 532 nm excitation laser, have the main peak at $\upsilon(H_2)$ = 4140 cm^{-1} (123 GPa) whose pressure dependence $\nu(P)$ is very similar to the behavior of the molecular hydrogen vibron, and the intensity of this peak decreases with increasing pressure. This value of $\upsilon(H_2)$ is slightly higher than for pure hydrogen under pressure, but a similar situation was observed earlier for NaH_7[18] and LiH_6.[31] The one-phonon resonant Raman calculations for $P1$-SrH_{22} at 120 GPa (Figure S29, Supporting Information) give the main signal at 4154 cm^{-1}, in close agreement with the experiment, whereas the nonresonant calculations predict several strong signals <4100 cm^{-1} which are not observed. Careful calculations show that all these Raman peaks have practically zero intensity.

Another strontium hydride, metastable Sr_3H_{13}, crystallizes in the monoclinic space group $C2/m$. A unique property of this compound is the presence of zigzag H_5 molecules with almost constant distance d(H−H) = 0.9–1.0 Å. Calculations of the band structure indicate that this material exhibits metallic properties and should have a superconducting transition temperature $T_C \approx 84$ K at 150 GPa (μ^* = 0.1, Figure S9, Supporting Information). A decrease in pressure in DAC Sr2 from 146 to 70 GPa demonstrates that monoclinic Sr_3H_{13} remains stable in this pressure range, whereas SrH_{22} superhydride decomposes below 100 GPa.

2.2. High-Pressure Synthesis of Pseudocubic SrH_6

At the next stage of the study, we reduced the pressure of synthesis and examined DAC Sr3 (Table S1, Supporting Information) with 100 μm culet, loaded with ammonia borane (AB), gold foil (Au), and a strontium particle. Golden film was placed between AB and Sr to isolate them from each other and prevent the formation of $Sr(AB)_2$ amidoborane. The sample was heated by a 1 μm IR fiber laser from the AB side at 123 GPa. After decompression to 48 GPa, the sample became transparent and demonstrated the Raman peaks at 3635 and 735 cm^{-1} (Figure S27, Supporting Information).

The observed X-ray diffraction pattern (**Figure 2**a,b) with main reflections (200), (210), and (211) corresponds to the $Pm\bar{3}n$ structure found earlier in the studies of europium (Eu_8H_{46}[24]) and barium (Ba_8H_{46}[25]) polyhydrides. However, both the harmonic and anharmonic calculations show dynamical instability at 300 K of structurally similar cubic strontium hydride Sr_8H_{46}, which distorts to $R\bar{3}c$ having a significantly different XRD pattern. For this reason, we performed an additional structural search for stable compounds with fixed Sr:H compositions of 2:12 and 8:48. As a result, we found thermodynamically and dynamically stable (Figure 1c,f) pseudocubic $P1$-Sr_8H_{48}, denoted for simplicity as $P1$-SrH_6, whose Sr sublattice differs

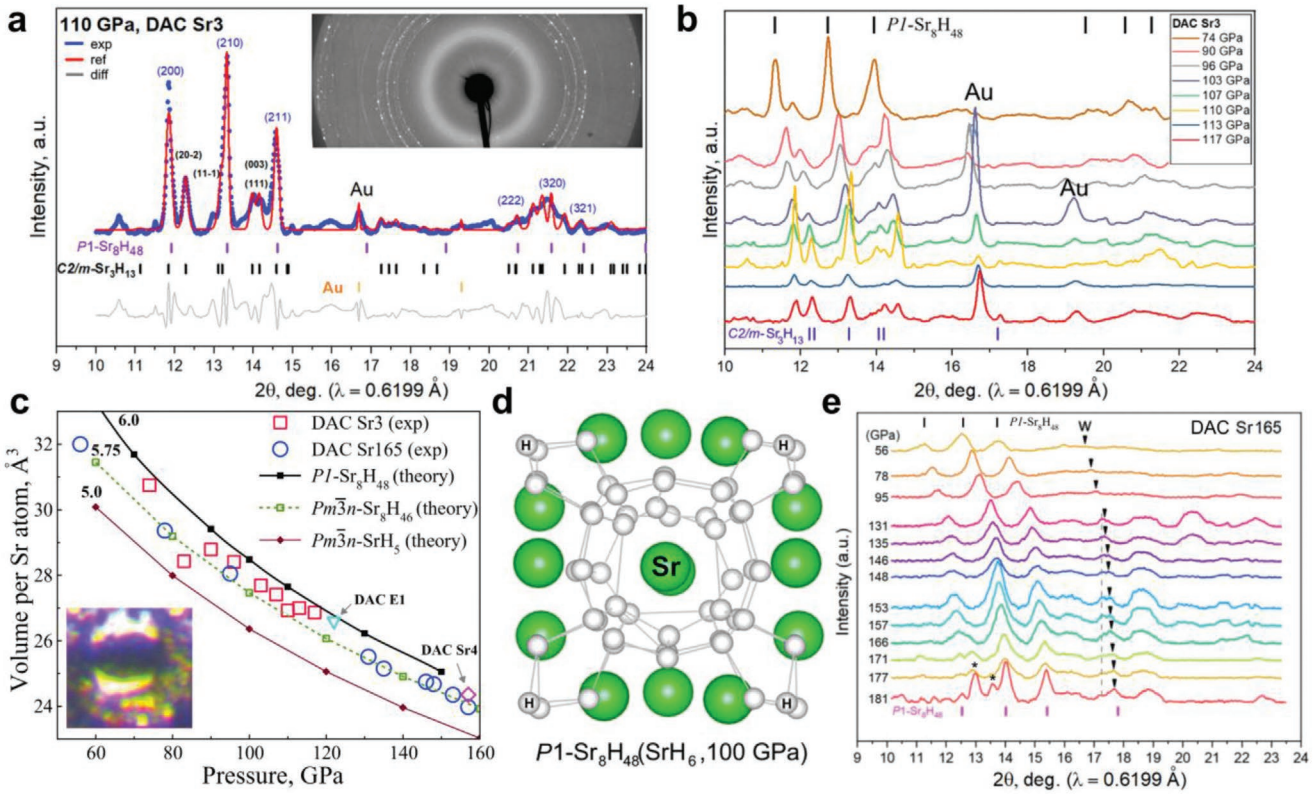

Figure 2. X-ray diffraction study of strontium hydrides in DACs Sr3 and Sr165. a) Experimental XRD pattern and Le Bail refinements of the unit cell parameters of $Pm\bar{3}n$-like pseudocubic $P1$-SrH_6 and $C2/m$-Sr_3H_{13} at 110 GPa. The experimental data, fit, and residues are shown in blue, red, and gray, respectively. Inset shows the 2D diffraction image. b) XRD patterns measured during the decompression of DAC Sr3 from 117 to 74 GPa. During the XRD experiment, the sample was shifted, thus we can see various relative intensities of Au. c) Experimental and theoretical pressure dependences of the unit cell volume for $P1$-SrH_6, $Pm\bar{3}n$-Sr_8H_{46}, and SrH_5. Inset: Photo of the sample in DAC Sr165 at 160 GPa after the laser heating in transmitted and reflected light. d) Crystal structure of $P1$-SrH_6 at 100 GPa. e) XRD patterns obtained during the decompression of DAC Sr165 from 181 to 56 GPa. The signals at $2\theta > 18°$ do not change with pressure and do not belong to the sample.

from that of $Pm\bar{3}n$-Sr_8H_{46} by only a slight distortion and has an almost identical XRD pattern. A slightly larger calculated cell volume of $\Delta V \approx 0.5$ Å^3 in comparison with experimental data (Figure 2c) can be explained by inaccuracy of the density functional theory (DFT) methods or nonstoichiometric composition of the hydride (e.g., Sr_8H_{47}). The experiment shows that the obtained $Pm\bar{3}n$-like phase is stable to at least 74 GPa. In addition to Sr_8H_{48}, this sample probably also contains an admixture of the previously described $C2/m$-Sr_3H_{13}.

At 100 GPa, Sr_8H_{48} crystallizes in the triclinic system with space group $P1$. The Sr—H bond length is 2.04–2.31 Å and the minimum H—H bond length is 0.84–0.87 Å. According to theoretical calculations, $P1$-SrH_6 is a narrow-bandgap semiconductor (Figures S16 and S17, Supporting Information) whose bandgap increases as pressure lowers. This may explain the fact that at pressures near or above 100 GPa the sample is opaque, whereas transparent regions and several Raman signals appear when pressure decreases (Figure S27, Supporting Information). To study conductivity in $P1$-SrH_6, we made an electrical DAC E1 (Table S1, Supporting Information) described further in the article.

The same pseudocubic $P1$-SrH_6 with a $Pm\bar{3}n$-like Sr sublattice was obtained in the experiment in high-pressure DAC Sr165 (Table S1, Supporting Information) with a 50 µm culet, in which the loaded Sr/AB sample ($d \approx 15$ µm) was heated by a laser to 1500–1800 K at 165 GPa. At this pressure, the synthesized compound is almost opaque, whereas below 56 GPa the sample became translucent (Figure S32, Supporting Information). During the subsequent decompression from 181 to 56 GPa, a series of low-intensity XRD patterns was obtained (Figure 2e). The analysis of these patterns points to pseudocubic $P1$-SrH_6 as the main component. The obtained hydride has a surprisingly high stability: the character of the XRD pattern does not change down to 56 GPa, in agreement with ab initio thermodynamic calculations (Figures S1 and S2, Supporting Information). In principle, this suggests that polyhydrides can maintain their structure during decompression, as has been recently shown for FeSe.[32]

2.3. Electrical Measurements of SrH_6

Electrical measurements for strontium hydrides are hindered by their low conductivity. The active resistance of samples at low frequencies is about several megohms; however, the use of high-frequency current up to 10 MHz makes it possible to obtain high-quality impedance patterns. We studied in detail the electrical DAC E1 with a pseudo-four-contact van der Pauw

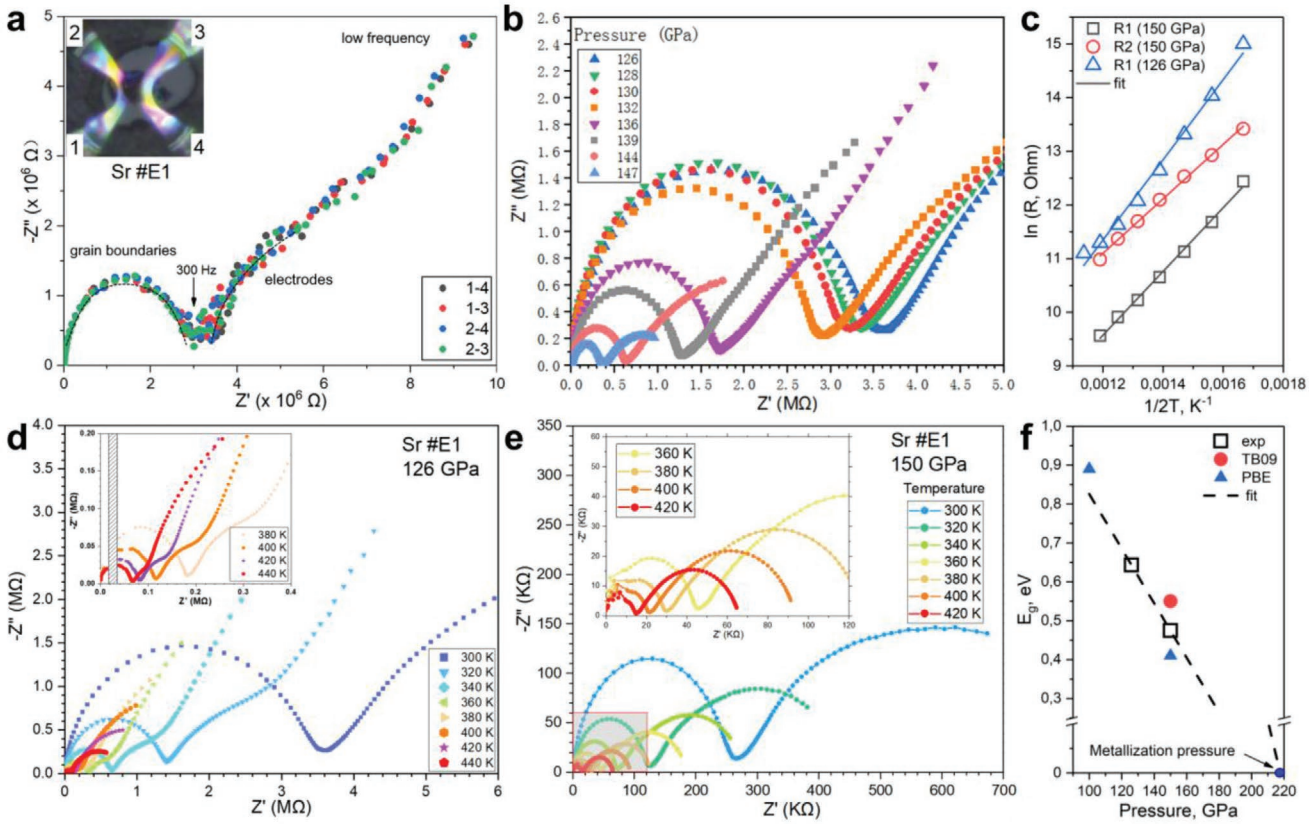

Figure 3. Impedance spectroscopy (Nyquist diagrams) of the pseudocubic *P*1-SrH_6 sample (DAC E1) in the frequency range from 0.1 to 10^7 Hz. a) The active resistance of the sample is 2.5 MΩ, the capacitance of the circuit is ≈0.5 μF with any combination of contacts. b) Impedance at pressures of 126–147 GPa and 300 K. c) Calculating the activation energy E_g using the temperature dependence of the electrical resistance. d,e) Impedance in the temperature interval of 300–440 K at 126 GPa (d), and in the range of 300–420 K at 150 GPa (e). f) Activation energy E_g compared to the direct bandgap of *P*1-SrH_6 at 100–150 GPa. See Supporting Information for details.

circuit, loaded with Sr/AB and heated at 126 GPa. According to the XRD study, the opaque sample consists of $Pm\bar{3}n$-like pseudocubic *P*1-SrH_6 (Figure S26, Supporting Information).

Before the experiment, we checked that an impedance of the circuit is equal for any combination of contacts (**Figure 3**a). On a typical hodograph for the SrH_6 sample, there is a clear first semicircle, the radius of which has a pronounced dependence on the temperature and pressure (Figure 3b,d,e). In some cases, especially at high temperatures and pressures, a part of the second semicircle or, to be correct, half-ellipse, is visible which continues with an oblique low-frequency tail. The dimensions of the second half-ellipse also significantly decrease as the temperature and pressure rise.

To interpret the obtained experimental data, we used a simplified $L(C, R)$(CPE, R) scheme of five elements, where L reflects the inductance of the lead wires, (C, R) corresponds to ionic conductivity at the grain boundaries of the SrH_6 nanocrystals, and (CPE, R) describes the transport and hydrogen diffusion phenomena at the border of the Mo electrodes.[33–35]

Simple calculations show that in the formula for active resistance $R(T) = R_0 \times \exp(-E_g/2k_BT)$, the activation energy E_g approximately equals 0.44–0.51 eV at 150 GPa (the average value is 0.475 eV) and increases to 0.64 eV at 126 GPa. This agrees with the optical properties of the sample (its darkening) and the value of the DFT bandgap for *P*1-SrH_6, predicted to be 0.55 eV at 150 GPa (Figure S17, Supporting Information). Moreover, the pressure dependence allows us[36] to calculate dE_g/dP. The data from Figure 3b give $d\ln(R)/dP = -0.13$ GPa^{-1} and $dE_g/dP = -0.0067$ eV/GPa at 300 K. Thus, the expected metallization pressure of $Pm\bar{3}n$-like pseudocubic *P*1-SrH_6 is 220 GPa (Figure 3f).

We calculated the diffusion coefficients of hydrogen for SrH_6 and SrH_{22} at 150 GPa using machine learning interatomic potentials (MLIP, Table S2 and Figures S37, S38, and S45, Supporting Information). Extrapolation of the data to 300 K gives D_H = 0.18 $Å^2$ ns^{-1} for SrH_6 and a significantly larger D_H = 17 $Å^2$ ns^{-1} for SrH_{22}. However, direct simulation at 300 K gives higher diffusion coefficients: 7.7 and 20 $Å^2$ ns^{-1}, respectively. Thus, SrH_{22} is the first discovered polyhydride where apparently there is no ordered hydrogen sublattice. Estimates of ionic conductivity using the Nernst–Einstein (NE) relation give the following values for conductivity: $\sigma_{NE}(300\ K) \approx 10^{-3}$ S cm^{-1} and $\sigma_{NE}(500\ K) \approx 3.5 \times 10^{-2}$ S cm^{-1} for SrH_6 at 150 GPa, lower than the experimental σ_{exp} (400 K) ≥ 0.1 S cm^{-1}. Higher ionic conductivity is expected in SrH_{22}: $\sigma_{NE}(500\ K) \approx 0.2$ S cm^{-1} at 150 GPa, which allows us to consider this compound as a superionic hydride.

A better organized structure of *P*1-SrH_6, which is close to the cubic prototypes $Pm\bar{3}n$-Eu_8H_{46}[24] and Ba_8H_{46},[25] is more stable

than the disordered molecular hydride SrH_{22}, where individual hydrogen atoms and molecules can migrate to a neighboring unit cell within 1 ns. This surprising fact is confirmed by the radial distribution functions (Figures S39–S45, Supporting Information): both strontium hydrides have a glassy disordered H sublattice and a solid Sr sublattice, stabilized due to the interaction of coordination shells [SrH_{24}] at 300–600 K and 150 GPa. Calculations of the phonon band structure and elastic moduli in both cases indicate the absence of dispersion and almost complete isotropy of hydrogen sublattices, which exhibit properties of a glass or liquid. These properties make it possible to use strontium polyhydrides as a solid electrolyte for high-pressure electrochemical reactions.[37]

3. Conclusions

The importance of studying strontium polyhydrides stems from Sr being a promising element for the design of ternary and quaternary superconducting hydrides stable below 1 Mbar. Unlike Ca and Y, strontium forms binary superhydrides with a very high hydrogen content at relatively low pressures of 50–90 GPa. These compounds exhibit semiconducting behavior below 120–150 GPa, whereas calcium and yttrium superhydrides are high-T_C superconductors.

Complex and diverse behavior of the Sr—H system under pressure differs significantly from that of Ca—H, where CaH_4 and CaH_6 are present, and is closer to Ba—H in the chemical properties. In the Sr—H system, there is a series of molecular polyhydrides forming at pressures of 25–165 GPa: $Pm\bar{3}n$-like and $Im\bar{3}m$-like polymorphs of SrH_6, $F\bar{4}3m$-like $SrH_{\approx 9}$ (see Supporting Information), and pseudotetragonal $P1$-SrH_{22}. Using the impedance spectroscopy, we estimated the direct bandgap in the $Pm\bar{3}n$-like polymorph $P1$-SrH_6 to be 0.44–0.51 eV at 150 GPa and the metallization pressure of this hydride to be 220 GPa.

The most amazing strontium hydride we observed is pseudotetragonal superionic $P1$-SrH_{22}, the hydride of metal with the highest hydrogen content discovered so far, which can be considered a form of molecular hydrogen glass doped with 4 at% of Sr. This indicates the promise of studying strontium compounds for hydrogen storage. SrH_{22} is stable at a relatively low pressure of 100 GPa, and its metallization via the band overlap can be achieved during compression to ≈200 GPa. Observing metallization in pure hydrogen is still a very difficult task associated with the study of extremely small samples. Therefore, SrH_{22} can be used as a helpful model of the hydrogen behavior above 300–350 GPa, realized at 1–2 Mbar. In a similar manner, barium hydride BaH_{12} (or $Ba_{0.08}H_{0.92}$) that we have discovered earlier can be used as a model for the emergence of superconductivity in already metallic hydrogen.

4. Experimental Section

Experimental Details: To synthesize the predicted strontium hydrides, we prepared several diamond anvil cells (DACs): Sr1–4, Sr50, Sr90, Sr165, and an electrical cell E1. We used diamond anvils with a 50–100 μm culet beveled to 250–300 μm at 8.5°. Strontium (>99.9%) particles with a diameter of 15–30 μm or SrH_2 powder (>99.9%) and sublimated ammonia borane (AB, >99.9%) were loaded into the tungsten gasket hole, with a thickness of 10–12 μm and a diameter of 35–60 μm, in an inert glove box. AB was used as a hydrogen source, following the technique that has shown excellent results in previous stu dies.[10,15,16,19,38] In DAC Sr3, the strontium particle was protected from reacting with AB by a thin gold foil ≈2 μm. Ammonia borane is a weak acid, therefore strontium may react with it upon contact during the DACs' loading. However, the salt $Sr(AB)_2$ that formed on the surface of the Sr particle decomposed with emission of H_2 during laser heating and did not interfere with the synthesis of hydrides. A special test on DACs Sr4 and E1 confirmed a uniform pressure distribution in the sample area (Figure S31, Supporting Information), with the accuracy of the pressure determination of ±6 GPa (4%). The heating of the Sr and SrH_2 samples above 1000 K at pressures of 70–170 GPa was carried out by several 0.1–0.5 s pulses of an IPG YLR infrared laser (1.07 μm), and led to formation of strontium polyhydrides.

The applied pressure was measured by the edge of diamond Raman signal[39] using a Horiba T64000 system with an exposure time of 10 s at 532 nm. The X-ray diffraction (XRD) patterns from samples in diamond anvil cells (DACs) were recorded on BL15U1 synchrotron beamline at the Shanghai Synchrotron Research Facility (SSRF, China) using a focused (5 × 12 μm) monochromatic X-ray beam with a linear polarization (20 keV, 0.6199 Å). Mar165 CCD was used as a detector.

The experimental XRD images were analyzed and integrated using Dioptas software package (version 0.5).[40] The full profile analysis of the diffraction patterns and the calculations of the unit cell parameters were performed in Materials studio[41] and JANA2006[42] using the Le Bail method.[43]

To investigate the electrical resistivity of strontium polyhydrides, we performed measurements in Cu—Be DACs E1 using the pseudo-four-probe technique. The tungsten gasket with an initial thickness of 250 μm was precompressed to 25 GPa. Then a hole with a diameter 20% larger than the culet diameter was drilled in the tungsten gasket using a pulse laser (λ = 532 nm). The cubic boron nitride (cBN) powder mixed with epoxy was used as an insulating layer. We filled the chamber with MgO and compressed it to 5 GPa. Then, in the obtained transparent MgO layer, a hole with a diameter of 40 μm was drilled by a laser. Ultraviolet lithography was used to prepare four electrodes on the diamond culet. We deposited the 500 nm thick Mo layer by magnetron sputtering (with the field of 200 V at 300 K) and removed excess metal by acid etching. Four deposited Mo electrodes were extended by a platinum foil, severally. The chamber was filled with sublimated ammonia borane (AB), and a small piece of Sr was placed on the culet of the upper diamond with four electrodes. All preparations were made in an argon glove box (O_2 < 0.1 ppm, H_2O < 0.01 ppm). After that, the DAC was closed and compressed to the required pressure.

Impedance spectroscopy was performed using Solartron SI 1260 impedance analyzer equipped with Solartron 1296 dielectric interface. A 100 mV sine signal with a sweep frequency from 0.1 to 10^7 Hz was irradiated on the sample. The symmetric BeCu cell was put on a thermostatic flat-plate heater for a higher temperature, which was recorded using a T-type thermocouple inserted into the cell.

A summary of the stability parameters of all studied compounds and DACs is presented in Table S1, Supporting Information.

Computational Details: The non-self-consistent and self-consistent calculations were performed using the DFT[44,45] within the Perdew–Burke–Ernzerhof functional (generalized gradient approximation)[46] as implemented in the Abinit code.[47,48] The computations of the total energy and optimization of the geometry of strontium hydrides were carried out using the optimized norm-conserving scalar-relativistic Vanderbilt pseudopotentials (ONCVPSP).[49] The kinetic energy cutoff for plane waves was found through the convergence tests for the total energy and the unit cell parameters performed in the interval from 5 to 80 Ha (ecut). The Brillouin zone was sampled using *k*-points meshes with a resolution found via the convergence tests for the total energy and the unit cell parameters performed in the interval from 1 × 1 × 1 to 8 × 8 × 8 (ngkpt). The band structure calculations were performed

using the Hartwigsen–Goedecker–Hutter nonrelativistic local-density approximation (LDA) pseudopotentials[50] with the kinetic energy cutoff of 30 Ha and a $4 \times 4 \times 4$ *k*-points mesh.

The non-self-consistent and self-consistent calculations of the equations of state and electron and phonon band structure of Sr_3H_{13} and SrH_{22} were performed using the DFT within the Perdew–Burke–Ernzerhof functional (generalized gradient approximation) as implemented in the Abinit and VASP codes. The Bader analysis was performed using Critic2 software.[51,52]

The dynamic stability and phonon density of states (DOS) of SrH_{22} were studied using classical molecular dynamics and the interatomic potential based on machine learning. We used the Moment Tensor Potential (MTP)[53] whose applicability in calculations of the phonon properties of materials has been demonstrated previously. Moreover, within this approach we can explicitly take into account the anharmonicity of hydrogen vibrations. To train the potential, we first simulated Sr hydrides in quantum molecular dynamics in an *NPT*-ensemble at 100 GPa and 10, 100, and 300 K, with a duration of 5 ps using the VASP code.[54–56] We used the PAW PBE pseudopotentials for the H and Sr atoms, and $2\pi \times 0.06$ Å^{-1} *k*-mesh with a cutoff energy of 400 eV. For training the MTP, sets of structures were chosen using active learning. We checked the dynamical stability of the studied Sr hydrides with the obtained MTPs via several runs of molecular dynamics calculations at 300 K and 180 GPa. First, the *NPT* dynamics simulations were performed in a supercell with ≈1000 atoms for 40 ps. During the last 20 ps, the cell parameters were averaged. In the second step, the coordinates of the atoms were averaged within the *NPT* dynamics with a duration of 20 ps and the final structures were symmetrized as implemented in T-USPEX method. Then, for the structures of Sr polyhydrides relaxed at 100 GPa and 10, 100, and 300 K, the phonon DOS was calculated using the velocity autocorrelator (VACF) separately for each type of atoms:

$$g(\theta) = 4\int_0^\infty \cos(2\pi\theta t)\frac{\overline{\langle V(0)V(t)\rangle}}{\langle V(0)^2\rangle}\mathrm{d}t \tag{1}$$

where θ is the frequency. The calculations were carried out in a $20 \times 20 \times 20$ supercell.

All Raman investigations were performed using Abinit v.9.4.1. At 120 GPa, *P*1-SrH_{22} is a metal with a band structure where the bands do not intersect with each other (see TB09 band structure). We optimized the crystal structure using the PBE DFT functional with the Fermi–Dirac distribution and a smearing temperature of 0.01 Ha. A Γ-centered *k*-point grid with a $6 \times 6 \times 6$ mesh was used. The obtained initial band structure showed no intersection between the valence and conduction bands in the Brillouin zone. Therefore, we can treat SrH_{22} as a semiconductor in the first approximation, fixing the number of the occupied bands, which allowed us to calculate the Raman spectra using the density functional perturbation theory for semiconductors.[57] In this case, we tested two different approaches using the same Γ-centered grid with $6 \times 6 \times 6$ *k*-points:

i) The crystal structure was optimized using the LDA DFT functional with norm-conserving pseudopotentials and its band structure generated using a non-self-consistent approach was compared with the band structure generated using the TB09 meta-GGA DFT functional.
ii) The crystal structure was optimized using the PBE DFT functional with norm-conserving pseudopotentials and its band structure generated using a non-self-consistent approach was compared with the band structure generated using the TB09 meta-GGA DFT functional.

In the first and second approaches, SrH_{22} was considered a semiconductor, maintaining the fixed band occupation. The subsequent one-phonon nonresonant Raman spectra were calculated using PEAD approach[57] and compared with the experimental one (Figure S29, Supporting Information). Both approaches give rather poor agreement with the experimental data, but the position of one of the groups of signals (≈4200 cm^{-1}) predicted in approach (ii) coincides with the experimental value.

Then, in more advanced one-phonon resonant Raman calculations, the Raman susceptibility was obtained from the derivative of the dielectric function for the incoming laser frequency (532 nm).[58,59] We considered the optimized crystal structure with the PBE and norm-conserving pseudopotentials for a metal with a Fermi–Dirac distribution and the temperature of smearing equal to 0.01 Ha to calculate the subsequent dynamical matrix (Δ) using the density functional perturbation theory with the LDA DFT functional and norm-conserving pseudopotentials. The right frequencies of metal *P*1-SrH_{22} were obtained solving the secular equation:

$$\Delta Q_\zeta = \omega_\zeta^2 Q_\zeta \tag{2}$$

where $Q_\zeta = (e_{1\zeta},...,e_{N\zeta})$ is the eigenvector (i.e., displacement) of the phonon mode ζ with a frequency ω_ζ, which in general consists of 3*N* components, where *N* is the number of atoms per unit cell. The intensity *I* of the Raman spectra at each phonon frequency mode ω_ζ for a photon of frequency ω_{laser} is defined as:

$$I = (\omega_{laser} - \omega_\zeta)^4 \left| e_{out} \cdot \alpha^\zeta \cdot e_{in} \right|^2 \frac{n_\zeta + 1}{2\omega_\zeta} \tag{3}$$

where $n_\zeta = \frac{1}{e^{\hbar\omega_\zeta/kT} - 1}$ is the phonon occupation factor that depends on the temperature *T*. Two ω_{laser} values were considered: 532 nm (green) and 650 nm (red), which can cover the energy of the bandgap seen in the electronic structure of *P*1-SrH_{22} calculated using the PBE DFT functional. The fundamental bandgap is 0.08 eV, the direct bandgap is 1.39 eV (Figures S10–S12, Supporting Information).

The term α^ζ in Equation (3) is defined as the Raman susceptibility:[57]

$$\alpha_{ij}^\zeta(\omega) = \sqrt{\Omega_0}\sum_{\tau\beta}\frac{\partial\chi_{ij}(\omega)}{\partial R_{\tau\beta}}u_{\tau\beta}^\zeta \tag{4}$$

where Ω_0 is the unit cell volume, χ_{ij} is the macroscopic dielectric susceptibility, and $u_{\tau\beta}^\zeta$ is the eigendisplacement of the phonon mode ζ of atom τ in the direction β. In the case of the Raman spectra of powders, the intensity of a peak at each frequency is the sum of the parallel intensity $I_{\parallel}^{powder}$ and perpendicular intensity $I_{\perp}^{powder}$, which can be defined as:

$$I_{\parallel}^{powder} = C(10G_0 + 4G_2) \tag{5}$$

$$I_{\perp}^{powder} = C(5G_1 + 3G_2) \tag{6}$$

$$I_{tot}^{powder} = I_{\parallel}^{powder} + I_{\perp}^{powder} \tag{7}$$

where

$$G_0 = \frac{(\alpha_{xx} + \alpha_{yy} + \alpha_{zz})^2}{3} \tag{8}$$

$$G_1 = \frac{(\alpha_{xy} - \alpha_{yz})^2 + (\alpha_{yz} - \alpha_{zx})^2 + (\alpha_{zx} - \alpha_{xy})^2}{2} \tag{9}$$

$$G_2 = \frac{(\alpha_{xy} + \alpha_{yz})^2 + (\alpha_{yz} + \alpha_{zx})^2 + (\alpha_{zx} + \alpha_{xy})^2}{2} + \frac{(\alpha_{xx} + \alpha_{yy})^2 + (\alpha_{yy} + \alpha_{zz})^2 + (\alpha_{zz} - \alpha_{xx})^2}{2} \tag{10}$$

$$C = (\omega_{laser} - \omega_\zeta)^4 \frac{n_\zeta + 1}{2\omega_\zeta} \tag{11}$$

We calculated I_{tot}^{powder} for the previously optimized structure of primitive triclinic SrH_{22} at 120 GPa using the PBE DFT functional and norm-conserving pseudopotentials. The macroscopic dielectric susceptibility χ_{ij} was calculated using the LDA DFT functional and norm-conserving pseudopotentials with 80 bands for the derivative of energy with respect to *k*-points within the Brillouin zone, and the Fermi–Dirac distribution of occupation with a smearing temperature of 0.01 Ha. A Γ-centered grid with $16 \times 16 \times 16$ *k*-points was used.

As a result, the Raman spectrum of SrH_{22} was significantly simplified: only three signals, ≈4000, 4150, and 4300 cm^{-1}, remained in the spectrum, the most intense of which corresponds well to the experimentally observed peak at 4140 cm^{-1} (123 GPa, 100 K). Another peak, lower than 4000 cm^{-1} and of much weaker intensity, is also seen in such one-phonon resonant Raman computations, but its intensity strongly depends on the match between the theoretical gap value and incoming laser frequency. Because of the absence of a pressure dependence, we assume that the experimental Raman signals at ≈4500 and 4800 cm^{-1} do not belong to the sample.

We estimated the diffusion rate in strontium hydrides using classical molecular dynamics with a machine learning interatomic potential implemented in the MLIP package.[53,60,61] The interatomic potential was actively trained on the ab initio molecular dynamics trajectories of SrH_6 and SrH_{22} unit cells in the *NPT*-ensemble (P = 150 GPa, T = 1000 K) with the external electric field of 10^4 V m^{-1} applied in the [100] direction. The reference ab initio data on energies, forces, and stresses were obtained on the DFT level using the VASP code.[54–56] We used the following VASP settings for training set preparation: the cutoff energy of the plane waves basis set was 450 eV, the first Brillouin zone was sampled by a Gamma-centered grid with $2\pi \times 0.03$ $Å^{-1}$ resolution, and the partial occupancies of electron states were set using a Gaussian method with 0.05 eV smearing width. The convergence criteria of the Self Consistent Field (SCF) cycle was 10^{-5} eV. The resulting actively selected training set had 2012 configurations, and the mean absolute errors (MAE) of the prediction of these configurations' energies and forces were 4.8 meV per atom and 0.27 eV $Å^{-1}$ (≈25%), respectively. Molecular dynamics simulation in VASP for 30 ps shows discontinuous movement of H atoms; from this data, it is impossible to draw a clear conclusion about the diffusion parameters of the system.

The obtained interatomic potential was used to perform a large-scale molecular dynamics run on a $4 \times 4 \times 4$ supercell of SrH_{22} and $3 \times 3 \times 3$ supercell of Sr_8H_{48} at temperatures of 500, 550, and 600 K and a constant pressure of 150 GPa using LAMMPS package.[62] Each run lasted within 300 ps with a time step of 0.3 fs. Additionally, the external electric field of 10^6 V m^{-1} was applied to each system. Estimates of ionic conductivity using the Nernst–Einstein relation gave the following results: σ(300 K) ≈ 10^{-3} S cm^{-1} and σ(500 K) ≈ 3.5×10^{-2} S cm^{-1} for SrH_6 at 150 GPa. Higher ionic conductivity is expected in SrH_{22}:σ(500 K) ≈ 0.2 S cm^{-1} at 150 GPa, which allows us to consider this compound as a superionic hydride.

The initial atomic charges of the Sr and H atoms were obtained using the Bader charge analysis (Tables S9, S16, and S17, and Figures S14, S37, and S38, Supporting Information) of the DFT ground state charge distributions of SrH_6 and SrH_{22} hydrides and kept fixed during the simulation. The Bader analysis of the simulations in VASP after 30 ps indicates that the charges on atoms change insignificantly (Figures S37 and S38, Supporting Information). Finally, the diffusion coefficients of hydrogen atoms in the [100] direction were calculated using the Einstein formula (projection on x): $x^2 = 2Dt$. An activation formula $D(T) = D_0 \times \exp(-E_a/k_BT)$ was used to extrapolate the temperature dependence of the diffusion coefficients (from 500–600 to 300 K, Table S2, Supporting Information). In the order of magnitude, the obtained diffusion coefficients agree with the results of other works.[63]

Supporting Information

Supporting Information is available from the Wiley Online Library or from the author.

Acknowledgements

In situ angle dispersive XRD experiments were performed at 15U1 beamline, Shanghai Synchrotron Radiation Facility (SSRF). This work was supported by the National Key R&D Program of China (No. 2018YFA0305900), National Natural Science Foundation of China (Nos. 52072188, 51632002, and 11974133), and Program for Changjiang Scholars, Innovative Research Team in University (No. IRT_15R23). A.R.O. thanks the Russian Science Foundation (grant 19-72-30043). D.V.S. thanks the Russian Foundation for Basic Research (project 20-32-90099) and the Russian Science Foundation (grant 22-22-00570). I.A.K. and A.B.M. thank the Russian Science Foundation (grant No. 21-73-10261) for the financial support of the anharmonic phonon density of states calculations and diffusion simulations. C.T. performed the calculations on resources provided by Sigma2 - the National Infrastructure for High Performance Computing Data Storage in Norway. C.T. acknowledges funding from Russian state assignment to ISSCM SB RAS (project no. FWUS-2021-0005). X.G. acknowledges funding from the FRS-FNRS Belgium under grant number T.0103.19 – ALPS. The authors also thank Igor Grishin (Skoltech) for proofreading the manuscript, Monan Ma (BU) for the laser heating simulations in COMSOL, and Song Hao (Jilin University) for helping to interpret the very first experiments with strontium hydrides in 2019.

Conflict of Interest

The authors declare no conflict of interest.

Author Contributions

D.V.S. and W.C. contributed equally to this work. W.C., X.H., and T.C. performed all experiments with diamond anvil cells. D.V.S., W.C., and X.H. analyzed and interpreted the results of the XRD, impedance, and optical measurements, and D.V.S. wrote the manuscript. X.H., A.R.O., and T.C. directed the research and edited the manuscript. I.A.K. and A.B.M. performed the T-USPEX and anharmonic phonon density of states calculations and MLIP-LAMMPS diffusion simulations. M.G. wrote Python scripts for accelerated USPEX data processing and automatic interpretation of diffraction patterns. A.G.K., D.Z., and A.R.O. prepared the theoretical analysis and calculated the equation of states and electron and phonon band structures for various strontium hydrides. C.T. and X.G. performed the Bader analysis, ABINIT band structure calculations with TB09 and PBE, dielectric function calculations, and nonresonant (PEAD) and resonant Raman spectrum calculations. All the authors provided critical feedback and helped shape the research.

Data Availability Statement

The raw and processed data required to reproduce these findings are available to download from GitHub at https://github.com/mark6871/SrH22-Advanced-Materials-2022-, and as Supporting Information to the manuscript.

Keywords

high-pressure electrochemistry, hydrogen, superconductivity, superhydrides

Received: January 27, 2022
Revised: April 4, 2022
Published online: June 3, 2022

[1] P. Loubeyre, F. Occelli, P. Dumas, *Nature* **2020**, *577*, 631.
[2] L. Monacelli, I. Errea, M. Calandra, F. Mauri, *Nat. Phys.* **2021**, *17*, 63.
[3] M. I. Eremets, A. P. Drozdov, P. P. Kong, H. Wang, *Nat. Phys.* **2019**, *15*, 1246.
[4] R. J. Hemley, H. K. Mao, *Science* **1989**, *244*, 1462.
[5] R. P. Dias, I. F. Silvera, *Science* **2017**, *355*, 715.
[6] A. P. Drozdov, M. I. Eremets, I. A. Troyan, V. Ksenofontov, S. I. Shylin, *Nature* **2015**, *525*, 73.
[7] X. Huang, X. Wang, D. Duan, B. Sundqvist, X. Li, Y. Huang, H. Yu, F. Li, Q. Zhou, B. Liu, T. Cui, *Natl. Sci. Rev.* **2019**, *6*, 713.
[8] A. P. Drozdov, P. P. Kong, V. S. Minkov, S. P. Besedin, M. A. Kuzovnikov, S. Mozaffari, L. Balicas, F. F. Balakirev, D. E. Graf, V. B. Prakapenka, E. Greenberg, D. A. Knyazev, M. Tkacz, M. I. Eremets, *Nature* **2019**, *569*, 528.
[9] M. Somayazulu, M. Ahart, A. K. Mishra, Z. M. Geballe, M. Baldini, Y. Meng, V. V. Struzhkin, R. J. Hemley, *Phys. Rev. Lett.* **2019**, *122*, 027001.
[10] I. A. Troyan, D. V. Semenok, A. G. Kvashnin, A. V. Sadakov, O. A. Sobolevskiy, V. M. Pudalov, A. G. Ivanova, V. B. Prakapenka, E. Greenberg, A. G. Gavriliuk, I. S. Lyubutin, V. V. Struzhkin, A. Bergara, I. Errea, R. Bianco, M. Calandra, F. Mauri, L. Monacelli, R. Akashi, A. R. Oganov, *Adv. Mater.* **2021**, *33*, 2006832.
[11] P. Kong, V. S. Minkov, M. A. Kuzovnikov, A. P. Drozdov, S. P. Besedin, S. Mozaffari, L. Balicas, F. F. Balakirev, V. B. Prakapenka, S. Chariton, D. A. Knyazev, E. Greenberg, M. I. Eremets, *Nat. Commun.* **2021**, *12*, 5075.
[12] E. Snider, N. Dasenbrock-Gammon, R. McBride, X. Wang, N. Meyers, K. V. Lawler, E. Zurek, A. Salamat, R. P. Dias, *Phys. Rev. Lett.* **2021**, *126*, 117003.
[13] D. V. Semenok, A. G. Kvashnin, A. G. Ivanova, V. Svitlyk, V. Y. Fominski, A. V. Sadakov, O. A. Sobolevskiy, V. M. Pudalov, I. A. Troyan, A. R. Oganov, *Mater. Today* **2020**, *33*, 36.
[14] W. Chen, D. V. Semenok, X. Huang, H. Shu, X. Li, D. Duan, T. Cui, A. R. Oganov, *Phys. Rev. Lett.* **2021**, *127*, 117001.
[15] D. Zhou, D. V. Semenok, D. Duan, H. Xie, W. Chen, X. Huang, X. Li, B. Liu, A. R. Oganov, T. Cui, *Sci. Adv.* **2020**, *6*, eaax6849.
[16] D. Zhou, D. V. Semenok, H. Xie, X. Huang, D. Duan, A. Aperis, P. M. Oppeneer, M. Galasso, A. I. Kartsev, A. G. Kvashnin, A. R. Oganov, T. Cui, *J. Am. Chem. Soc.* **2020**, *142*, 2803.
[17] C. Pépin, P. Loubeyre, F. Occelli, P. Dumas, *Proc. Natl. Acad. Sci. USA* **2015**, *112*, 7673.
[18] V. V. Struzhkin, D. Y. Kim, E. Stavrou, T. Muramatsu, H.-K. Mao, C. J. Pickard, R. J. Needs, V. B. Prakapenka, A. F. Goncharov, *Nat. Commun.* **2016**, *7*, 12267.
[19] W. Chen, D. V. Semenok, A. G. Kvashnin, X. Huang, I. A. Kruglov, M. Galasso, H. Song, D. Duan, A. F. Goncharov, V. B. Prakapenka, A. R. Oganov, T. Cui, *Nat. Commun.* **2021**, *12*, 273.
[20] E. Wigner, H. B. Huntington, *J. Chem. Phys.* **1935**, *3*, 764.
[21] A. R. Oganov, C. W. Glass, *J. Chem. Phys.* **2006**, *124*, 244704.
[22] A. R. Oganov, A. O. Lyakhov, M. Valle, *Acc. Chem. Res.* **2011**, *44*, 227.
[23] A. O. Lyakhov, A. R. Oganov, H. T. Stokes, Q. Zhu, *Comput. Phys. Commun.* **2013**, *184*, 1172.
[24] D. V. Semenok, D. Zhou, A. G. Kvashnin, X. Huang, M. Galasso, I. A. Kruglov, A. G. Ivanova, A. G. Gavriliuk, W. Chen, N. V. Tkachenko, A. I. Boldyrev, I. Troyan, A. R. Oganov, T. Cui, *J. Phys. Chem. Lett.* **2021**, *12*, 32.
[25] M. Peña-Alvarez, J. Binns, M. Martinez-Canales, B. Monserrat, G. J. Ackland, P. Dalladay-Simpson, R. T. Howie, C. J. Pickard, E. Gregoryanz, *J. Phys. Chem. Lett.* **2021**, *12*, 4910.
[26] J. Hooper, T. Terpstra, A. Shamp, E. Zurek, *J. Phys. Chem. C* **2014**, *118*, 6433.
[27] M. Somayazulu, P. Dera, A. F. Goncharov, S. A. Gramsch, P. Liermann, W. Yang, Z. Liu, H.-K. Mao, R. J. Hemley, *Nat. Chem.* **2009**, *2*, 50.
[28] J. Binns, P. Dalladay-Simpson, M. Wang, G. J. Ackland, E. Gregoryanz, R. T. Howie, *Phys. Rev. B* **2018**, *97*, 024111.
[29] C. Tantardini, E. Benassi, *Dalton Trans.* **2018**, *47*, 5483.
[30] C. Tantardini, E. Benassi, *Phys. Chem. Chem. Phys.* **2017**, *19*, 27779.
[31] T. Matsuoka, K. Kuno, K. Ohta, M. Sakata, Y. Nakamoto, N. Hirao, Y. Ohishi, K. Shimizu, T. Kume, S. Sasaki, *J. Raman Spectrosc.* **2017**, *48*, 1222.
[32] L. Deng, T. Bontke, R. Dahal, Y. Xie, B. Gao, X. Li, K. Yin, M. Gooch, D. Rolston, T. Chen, Z. Wu, Y. Ma, P. Dai, C.-W. Chu, *Proc. Natl. Acad. Sci. USA* **2021**, *118*, e2108938118.
[33] J. T. S. Irvine, D. C. Sinclair, A. R. West, *Adv. Mater.* **1990**, *2*, 132.
[34] X. Zhang, X. Wang, Q. Wang, X. Ma, C. Liu, P. Li, C. Liu, Y. Han, Y. Ma, C. Gao, *Phys. Chem. Chem. Phys.* **2018**, *20*, 8917.
[35] M. C. Verbraeken, C. Cheung, E. Suard, J. T. S. Irvine, *Nat. Mater.* **2015**, *14*, 95.
[36] R. Li, Y. H. Guo, B. Xu, Y. Su, J. Yin, C. H. Zhang, Y. D. Xia, Z. G. Liu, Z. Xu, L. C. Wu, Z. T. Song, *AIP Adv.* **2011**, *1*, 042115.
[37] P.-W. Guan, R. J. Hemley, V. Viswanathan, *Proc. Natl. Acad. Sci. USA* **2021**, *118*, e2110470118.
[38] D. V. Semenok, I. A. Troyan, A. G. Ivanova, A. G. Kvashnin, I. A. Kruglov, M. Hanfland, A. V. Sadakov, O. A. Sobolevskiy, K. S. Pervakov, I. S. Lyubutin, K. V. Glazyrin, N. Giordano, D. N. Karimov, A. L. Vasiliev, R. Akashi, V. M. Pudalov, A. R. Oganov, *Mater. Today* **2021**, *48*, 18.
[39] Y. A. H. Kawamura, *J. Phys.: Conf. Ser.* **2010**, *215*, 012195.
[40] C. Prescher, V. B. Prakapenka, *High Pressure Res.* **2015**, *35*, 223.
[41] P. Paufler, *The Rietveld Method. International Union of Crystallography* (Ed: R. A. Young), Oxford University Press, Oxford, UK **1993**, p. 298; *Cryst. Res. Technol.* **1995**, *30*, 494.
[42] V. Petříček, M. Dušek, L. Palatinus, *Z. Kristallogr.* **2014**, *229*, 345.
[43] A. Le Bail, *Powder Diffr.* **2005**, *20*, 316.
[44] P. Hohenberg, W. Kohn, *Phys. Rev.* **1964**, *136*, B864.
[45] W. Kohn, L. J. Sham, *Phys. Rev.* **1965**, *140*, A1133.
[46] J. P. Perdew, K. Burke, M. Ernzerhof, *Phys. Rev. Lett.* **1996**, *77*, 3865.
[47] X. Gonze, B. Amadon, P.-M. Anglade, J.-M. Beuken, F. Bottin, P. Boulanger, F. Bruneval, D. Caliste, R. Caracas, M. Côté, T. Deutsch, L. Genovese, P. Ghosez, M. Giantomassi, S. Goedecker, D. R. Hamann, P. Hermet, F. Jollet, G. Jomard, S. Leroux, M. Mancini, S. Mazevet, M. J. T. Oliveira, G. Onida, Y. Pouillon, T. Rangel, G.-M. Rignanese, D. Sangalli, R. Shaltaf, M. Torrent, et al., *Comput. Phys. Commun.* **2009**, *180*, 2582.
[48] X. Gonze, B. Amadon, G. Antonius, F. Arnardi, L. Baguet, J.-M. Beuken, J. Bieder, F. Bottin, J. Bouchet, E. Bousquet, N. Brouwer, F. Bruneval, G. Brunin, T. Cavignac, J.-B. Charraud, W. Chen, M. Côté, S. Cottenier, J. Denier, G. Geneste, P. Ghosez, M. Giantomassi, Y. Gillet, O. Gingras, D. R. Hamann, G. Hautier, X. He, N. Helbig, N. Holzwarth, Y. Jia, et al., *Comput. Phys. Commun.* **2020**, *248*, 107042.
[49] D. R. Hamann, *Phys. Rev. B* **2013**, *88*, 085117.
[50] C. Hartwigsen, S. Goedecker, J. Hutter, *Phys. Rev. B* **1998**, *58*, 3641.
[51] A. Otero-De-La-Roza, M. A. Blanco, A. M. Pendás, V. Luaña, *Comput. Phys. Commun.* **2009**, *180*, 157.
[52] A. Otero-De-La-Roza, E. R. Johnson, V. Luaña, *Comput. Phys. Commun.* **2014**, *185*, 1007.
[53] A. V. Shapeev, *Multiscale Model. Simul.* **2016**, *14*, 1153.
[54] G. Kresse, J. Hafner, *Phys. Rev. B* **1993**, *48*, 13115.
[55] G. Kresse, J. Hafner, *Phys. Rev. B* **1994**, *49*, 14251.
[56] G. Kresse, J. Furthmüller, *Phys. Rev. B* **1996**, *54*, 11169.
[57] M. Veithen, X. Gonze, P. Ghosez, *Phys. Rev. B* **2005**, *71*, 125107.

[58] P. Knoll, C. Ambrosch-Draxl, in *Anharmonic Properties of High Tc Cuprates*, *220*, World Scientific, Singapore **1995**.
[59] Y. Gillet, M. Giantomassi, X. Gonze, *Phys. Rev. B* **2013**, *88*, 094305.
[60] E. V. Podryabinkin, A. V. Shapeev, *Comput. Mater. Sci.* **2017**, *140*, 171.
[61] K. Gubaev, E. V. Podryabinkin, G. L. W. Hart, A. V. Shapeev, *Comput. Mater. Sci.* **2019**, *156*, 148.
[62] S. Plimpton, *J. Comput. Phys.* **1995**, *117*, 1.
[63] J. Binns, A. Hermann, M. Peña-Alvarez, M.-E. Donnelly, M. Wang, S. I. Kawaguchi, E. Gregoryanz, R. T. Howie, P. Dalladay-Simpson, *Sci. Adv.* **2021**, *7*, eabi9507.